Design and Analysis of Wide Speed Regulation of Variable Leakage Flux Reverse Salient-pole Motor

Xiping Liu, Siting Zhu, Dabin Liu, and Jianwei Liang

Abstract— **In this article, a new variable leakage flux reverse salient-pole motor (VLF-RSPM) is raised to widen the speed range. The innovation is to realize both reverse salient-pole characteristics and variable leakage flux characteristics by using a method of adding magnetic bridges and magnetic barriers. Firstly, the evolution of the topological structure and working principle of the motor are introduced. Secondly, based on 2D Finite Element Analysis (FEA), the electromagnetic properties and noise of the motor are analyzed in detail, and the electromagnetic properties are contrasted with that of the conventional V-type synchronous motor (CVTSM). The results show that VLF-RSPM has the advantages of small torque ripple, strong magnetic weakening ability, low noise, high efficiency, and low risk of permanent magnet demagnetization under different conditions. In addition, it is verified that the proposed motor extends the speed range.**

Index Terms—**Reverse salient-pole, Variable leakage flux, FEA, Wide speed range.**

I. INTRODUCTION

IN order to solve the serious energy crisis and environmental pollution caused by fuel vehicles [1], electric vehicles (EV) have been developed rapidly. The key to the high performance of EV lies in the drive motor, among which the most widely used drive motor is the permanent magnet motor, mainly because of its high efficiency, high-output torque, high power density, and good dynamic performance [2], [3]. However, because of the inherent properties of permanent magnet (PM) material of permanent magnet synchronous motor (PMSM) [4], it is difficult to adjust its internal magnetic field, causing the speed regulation range of the motor in the field weakening area is narrow. To expand the speed range of motor operation, a large d-axis current (id) is usually injected into the d-axis to weaken PM. However, adding id will inevitably increase copper loss and increase the irreversible demagnetization risk (IDR) of PMs [5]-[7].

Manuscript received May 10, 2022; revised August 10, 2022, and December 06, 2022 ; accepted February 20, 2023. Date of publication September 25, 2023; date of current version June 06, 2023.

This work was supported by National Natural Science Foundation of China Grant No. 52067008, in part by China Jiangxi Provincial Planning Project Grant No. 20181BAB206035, and in part by Qingjiang Excellent Young Talents Program, Jiangxi University of Science and Technology (JXUST).

Xiping Liu, Siting Zhu, Dabin Liu and Jianwei Liang are with the Jiangxi University of Science and Technology, Ganzhou 341000, China (e-mail: 2326529401@qq.com).

(Corresponding Author: Siting Zhu)

Digital Object Identifier 10.30941/CESTEMS.2023.00031

In recent years, many scholars have proposed variable leakage flux motors (VLFM) to expand the operating speed range. In [8]-[10], a hybrid excitation motor is proposed, which can flexibly adjust the PM magnetic field by changing the amplitude and current angle of the added excitation current, thereby expanding the speed regulation range. In [11], [12], scholars have proposed the memory motor, which mainly degaussed and demagnetized PM by injecting pulse current for a short time, thus realizing flux control and achieving high efficiency and wide speed range. The pulse current regulating the magnetization state of PM is generated by the DC magnetization coil [13], which is more convenient to control the magnetization state. Professor R. D. Lorenz of the United States proposed a flux-enhanced permanent magnet synchronous motor (FEPMS) [14], [15], which can reduce q-axis inductance (L_q) by adding a reasonable magnetic barrier on the q-axis of the rotor and increased the d-axis inductance (L_d) by adding a magnetic bridge on the d-axis of the rotor, to obtain reverse salient-pole characteristics ($L_d > L_q$). Due to the large L_d of the FEPMS, the id of the FEPMS is small when it runs at high speed, which can effectively reduce the IDR of PM [16]. Meanwhile, when it runs at low speed, id is positive because of the $L_d > L_q$ characteristics, it has a flux-intensifying effect on the air gap magnetic field, which reduces the irreversible demagnetization risk and enables wide speed regulation [17]. In [18], scholars proposed a controllable flux leakage permanent magnet motor (CLF-PM), which can expand the speed range by changing the rotor topology and adding one or more flux leakage paths.

A new variable leakage flux reverse salient-pole motor （VLF-RSPM） method is proposed in this paper. VLFRS-PM has the advantages of both the FEPMS and CLF-PM. Mainly by designing the topology of the motor rotor, the reverse salient-pole and variable leakage flux characteristics are realized. Then, a detailed analysis of each performance of the designed motor is carried out. The calculation results show that the design method can improve the expansion speed (ES) ability of the VLF-RSPM, but also sacrifice a lot of output torque.

II. TOPOLOGY AND PRINCIPLED OF MACHINE

A. Machine Topology

The comparison motor selected in this paper is shown in Fig. 1 (a), a conventional V-type synchronous motor (CVTSM).

The VLF-RSPM based on a comparison motor is proposed as shown in Fig. 1 (b). Their stator windings have the same structure with 8 poles and 48 slots, and the rotor structure is different. Fig. 2 shows how the rotor structure of CVTSM evolves step by step to a VLF-RSPM rotor structure. Firstly, an arc-shaped magnetic barrier and trapezoidal magnetic barrier are added to the *q*-axis magnetic circuit to form two leakage flux paths, blocking the downstream path of the q-axis, thereby reducing the self-magnetic flux leakage of PM. Meanwhile, they play the role of reducing L_q and providing paths for flux leakage variables under different working conditions. Secondly, segment PM to get a magnetic bridge that can increase the L_d. Finally, three magnetic barriers parallel to the *d*-axis are added to reduce the torque ripple, which vibration of the motor during operation, and also prevent the cross-coupling of the *d*-*q* axis. To sum up, through a series of innovative designs above, gets the target motor VLF-RSPM.

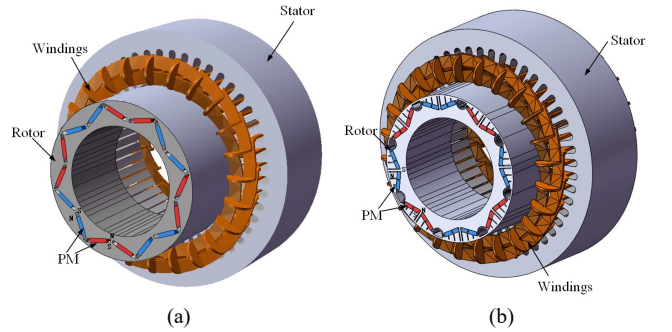

Fig. 1. Topologies diagram. (a) CVTSM. (b) VLF-RSPM.

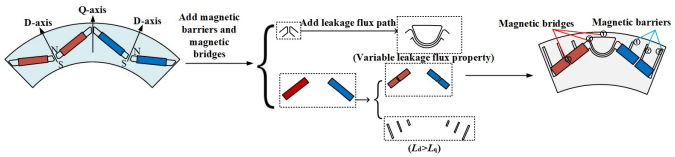

Fig. 2. The rotor structure of CVTSM evolves step by step to a VLF-RSPM rotor structure.

B. Operation Principles

In order to better distinguish the difference between the VLF-RSPM and the CVTSM, and better clarify the advantages of VLF-RSPM, the *d*-*q* axis magnetic circuits of the VLF-RSPM and the CVTSM are simplified as shown in Fig. 3 (a) and 3 (b). Since the magnetic circuit of VLF-RSPM has two more magnetic leakage paths and a magnetic bridge, it can be seen from the simplified magnetic circuit that VLF-RSPM has a leakage flux resistance in parallel with the d-axis magnetic circuit compared with CVTSM, and a leakage flux resistance is connected in series with the *q*-axis. Therefore, the L_q of the VLF-RSPM increases and the L_d decreases.

First, analyze $L_d > L_q$ characteristics; According to the simplified circuit diagram, while ignoring the influence of magnetic saturation and angular position, L_d and L_q can be expressed as

$$\begin{cases} L_d = \dfrac{N^2}{R_s + R_g + R_\delta \,\|\, (R_m + R_r)} \\ L_q = \dfrac{N^2}{R_s + R_g + R_m + R_r + R_\delta} \end{cases} \tag{1}$$

The number of turns of winding is *N*, and the resistances of the stator, the air gap, the leakage flux path, the PMs, and the magnetic barrier are R_s, R_g, R_δ, R_m, R_b, R_r, respectively. According to Equation (1), the characteristics of $L_d > L_q$ can be realized by adding magnetic bridges and magnetic barriers.

Finally, analyze the characteristics of variable leakage flux. According to Fig. 3 (b), the magnetomotive force of the PM, *d*-and-*q*-axis is F_{pm}, F_d, and F_q. the magnetic fluxes of the PM, stator, magnetic flux leakage path, and *q*-axis is Φ_{pm}, Φ_s, Φ_δ, and Φ_q, respectively. The variable leakage flux can be expressed as:

$$\begin{bmatrix} \Phi_{pm} \\ \Phi_s \end{bmatrix} = \frac{1}{\det R} \begin{bmatrix} R_s + R_g + R_\delta & R_\delta \\ R_\delta & R_r + R_\delta \end{bmatrix} \begin{bmatrix} F_{pm} \\ F_d \end{bmatrix} \tag{2}$$

Where

$$\begin{aligned} \det R &= \begin{vmatrix} R_s + R_g + R_\delta & R_\delta \\ R_\delta & R_r + R_\delta \end{vmatrix} \\ &= (R_s + R_g)R_r + (R_s + R_g + R_r)R_\delta \end{aligned} \tag{3}$$

$$\Phi_\delta = \Phi_{pm} - \Phi_s = \frac{(R_s + R_g)F_{pm} - R_r F_d}{\det R} \tag{4}$$

According to Equations (3) and (4), it can be found that Φ_δ depends on R_δ, that is, the Φ_δ depends on the size of the flux leakage paths. Furthermore, variable flux leakage characteristics can be obtained only if $\Phi_\delta \geq 0$. The key parameters of the VLF-RSPM and the CVTSM are shown in Table I.

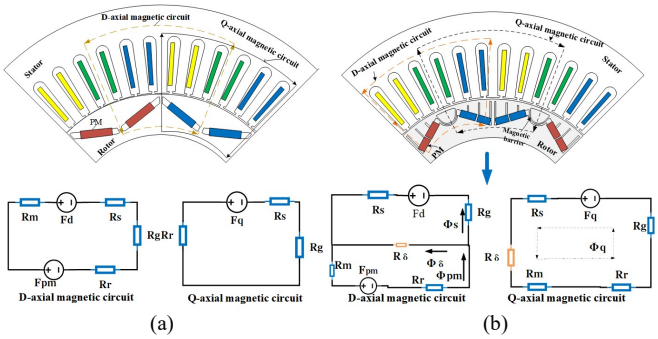

Fig. 3. Simplified equivalent circuit diagrams of a *d*-*q* axis. (a) CVTSM. (b) VLF-RSPM.

TABLE I
KEY DESIGN PARAMETERS OF THE TWO MOTORS

Items	VLF-RSPM	CVTSM
Rated output power (kW)	9	10
Rated phase current (A)	30	30
Air-gap length (mm)	0.75	0.75
Rated speed (rpm)	1000	1000
PM material	NdFe30	NdFe30
Stator inner diameter (mm)	161.9	161.9
Active stack length (mm)	83.82	83.82
Numbers of turns	21	21
Slots/Poles	48/8	48/8
PM width/ thickness (mm)	18.5/4.5	18.5/4.5

C. Design Parameters

To better analyze the VLF-RSPM, the VLF-RSPM is first optimized to obtain the best performance. Fig. 4 shows the

main parameters of the VLF-RSPM, where W_{fp1} and W_{fp2} are the widths of two magnetic flux leakage bridges. L_1, L_2, and L_3 are respectively the lengths of three parallel magnetic barriers, and T is their widths. L_{pm1} and L_{pm2} are the lengths of segmented PM. T_1 and T_2 are the widths of the magnetic bridge at the PM and d-axis, respectively. In addition, considering the performance of high torque, stability, and large speed expansion range required by the proposed VLF-RSPM, the torque, torque ripple and reverse salient ratio rate (L_d/L_q) is set as the optimization objectives.

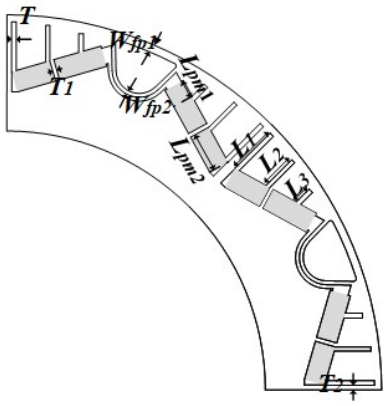

Fig. 4. Design variables of VLF-RSPM.

Since the number of variables is relatively large, and the influence on each optimization objective is different, to more effectively distinguish the relationship between each variable and each optimization objective, the sensitivity analysis method is applied in this paper, where the sensitivity index $S(x_i)$ is expressed as:

$$S(x_i) = \frac{V_a(E(g(x_i)/x_i))}{V_a(g(x_i))} \tag{5}$$

Where $E(g(x_i)/x_i)$ is the average value of optimization objective $g(x_i)$ when variable x_i is constant, and $V_a(E(g(x_i)/x_i))$ and $V_a(g(x_i))$ is the variances of $E(g(x_i)/x_i)$ and $g(x_i)$. The sensitivity index of each variable to each optimization objective is shown in Fig. 5, where the value determines the influence of the variable on the optimization objective, and the positive and negative value represents the positive or negative correlation between the parameter and the optimization objective. From Fig. 5, W_{fp1} has the greatest influence on the torque, followed by L_{pm1}, and the relationship between L_{pm1} and torque is positive. L_{pm1} has the greatest influence on torque ripple, and their relationship is positively correlated. L_{pm1} also has the greatest influence on the reverse salient ratio rate, but their relationship is negative, followed by L_1. It is found that each variable has different effects on each optimization objective, and they influence each other and also have conflicts. Therefore, it is difficult to determine the optimal design value of variable parameters by using the results of the sensitivity index. It is necessary to balance the relationship between each optimization objective to get the optimal result.

Based on the above sensitivity analysis, the main variables were determined, namely L_1, L_2, L_{pm1}, W_{fp1}, and T_1. The parameter ranges of the main variables were designed according to the rotor structure, as shown in Table II. Workbench and Maxwell co-simulation were used to optimize each variable.

In this paper, sequential nonlinear programming (SNP) is used to solve the optimal solution. Firstly, the boundary conditions are set as follows: torque greater than 80Nm, torque ripple less than 15%, and reverse salient ratio rate greater than 1.2. According to the constraints, the optimal solution can be effectively obtained by using SPN, as shown in Fig. 6. Table II shows the value of each parameter of the optimal point.

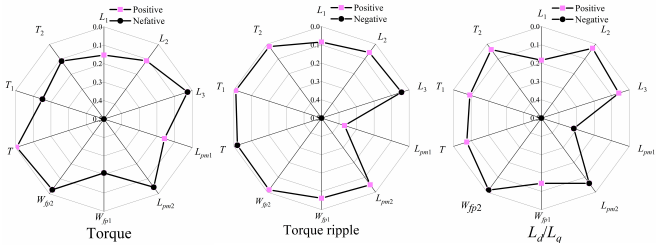

Fig. 5. Sensitivity analysis of design variables of VLF-RSPM.

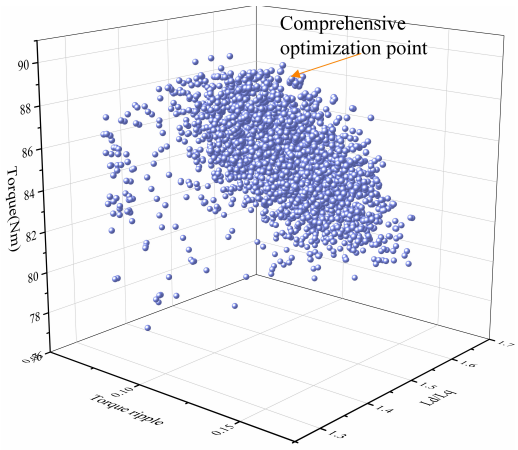

Fig. 6. Optimization results.

TABLE II
THE OPTIMIZATION RESULTS

Items	Variation parameters	Initial values	Optimized values
L_1 (mm)	[8.5-11]	10	10.68
L_2 (mm)	[6.5-8.5]	7	7.8
L_{pm1} (mm)	[6-12]	9	8.52
W_{fp1} (mm)	[77-79]	78	78.5
T_1 (mm)	[0.75-1.25]	0.9	0.8
Torque (Nm)	-	80	88
Torque ripple (%)	-	16	8
Reverse salient ratio rate	-	1.3	1.4

III. PERFORMANCES ANALYSIS AND COMPARISON

A. Magnetic Field Distribution

The magnetic field distribution of the CVTSM and the VLF-RSPM when the i_d is 30 A and the i_q is 30 A, respectively, are shown in Fig. 7. When the i_d is added, the magnetic lines of force passing through the stator are reduced, and the magnetic field is weakened, to achieve the purpose of expanding a wide

rotational speed range. Compare Fig. 7(a) with Fig. 7 (b), most of the magnetic field lines of VLF-RSPM pass through the leakage flux path to reduce the magnetic field and have better magnetic flux weakening ability. When the i_q is added, a large amount of PM flux passes through the stator, thereby generating torque, and it can be found from Fig. 4(b) that the magnetic field lines of the VLF-RSPM have no flux leakage under the condition of i_q=30 A, thus improve the PM torque. However, due to the design of VLF-RSPM, its maximum torque is smaller than that of CVTSM.

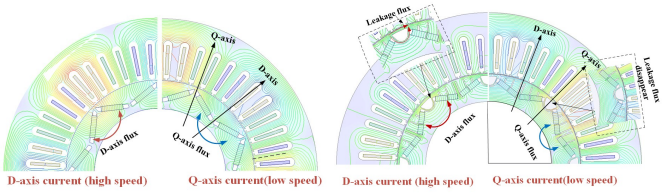

(a) (b)

Fig 7. Magnetic field distribution. (a) CVTSM. (b) VLF-RSPM.

In addition, to better analyze the variable flux leakage characteristics of the VLF-RSPM, the change of *d*-axis flux linkage with the increase of its i_q is analyzed as shown in Fig. 8. See from the figure, that when i_q = 0 A, many magnetic field lines pass through the magnetic leakage path, and the flux linkage of the *d*-axis is the smallest at this point. As the i_q increases, the magnetic flux of the *d*-axis also increases continuously, but it reaches the maximum when the current reaches 30 A, and then decreases with the increase of the i_q. Where $\Delta\Psi_{d\text{-}0}$ is the initial d-axis flux leakage, $\Delta\Psi_d$ is the maximum variable flux leakage, and K_Ψ is the maximum leakage flux rate of 24%.

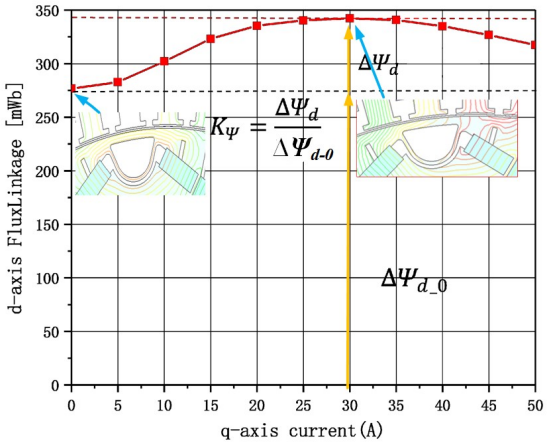

Fig 8. Relationship between *d*-axis Flux Linkage and *q*-axis current.

B. *Back-EMF and Air-gap Flux Density*

The air-gap is the main way to realize energy conversion of the motor, so it is very necessary for motor analysis. Fig. 9 (a) compares the air-gap flux density of the VLF-RSPM and the CVTSM, where VLF-RSPM has a slightly higher and sharper air-gap flux density peak. The no-load back-EMF of the VLF-RSPM and the CVTSM at a rated speed of 1000rpm in one electric angle cycle is shown in Fig. 9 (b). The back-EMF of VLF-RSPM is smaller, mainly because the magnetic leakage path of VLF-RSPM reduces the air-gap flux density. In addition, the harmonic analysis of no-load based on Fourier decomposition is shown in Fig. 9 (c), the VLF-RSPM has small harmonics of order 1, 3, 5, and 7, which indicates that the waveform of VLF-RSPM back-EMF is more sinusoidal. The air-gap flux density with more sinusoidal and smaller harmonic amplitude can reduce the torque ripple of the motor, which can effectively reduce the vibration and noise of the motor, improve the output torque, efficiency, and PM utilization of the motor, and is beneficial to control of the motor. and the more sinusoidal no-load back-EMF waveform is beneficial to motor control.

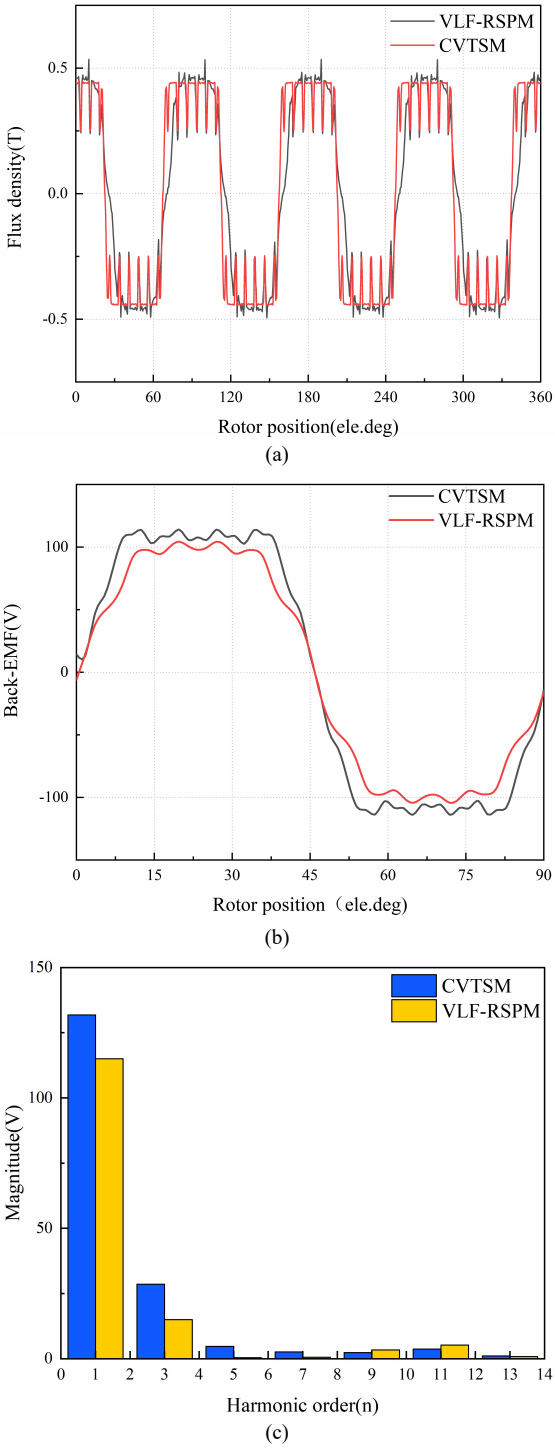

Fig 9. No-load performances. (a) Air-gap flux density. (b) Back-EMF. (c) Harmonic analysis of the back-EMFs.

C. Inductance Characteristics

Inductance plays an important role in the output torque, speed range, and flux attenuation of the motor, so it is necessary to analyze the L_d and L_q of the VLF-RSPM and the CVTSM. The inductance of the VLF-RSPM and the CVTSM under different current conditions when the current angle is set to 0 are presented in Fig. 10. It can be observed that the L_d and L_q of the VLF-RSPM and the CVTSM both decrease with the increase of the current, and the L_d decreases slowly, while the L_q decreases more rapidly. It can be seen from Fig. 10 (a) that the L_d<L_q characteristic of the CVTSM and the difference value between L_d and L_q become smaller as the current increases. Fig. 10 (b) shows the VLF-RSPM motor achieves the characteristics of L_d>L_q, and at the same time, L_d hardly decreases when the current is less than 20A and has the same decreasing speed as L_q when the current is greater than 20 A. By comparing the inductance of VLF-RSPM and CVTSM, it is found that the L_d of VLF-RSPM is larger than that of CVTSM and the L_q of VLF-RSPM is smaller than that of CVTSM, which is due to the magnetic bridge and magnetic barrier added to VLF-RSPM. The results show that adding magnetic bridges and magnetic barriers can realize the characteristics of L_d>L_q.

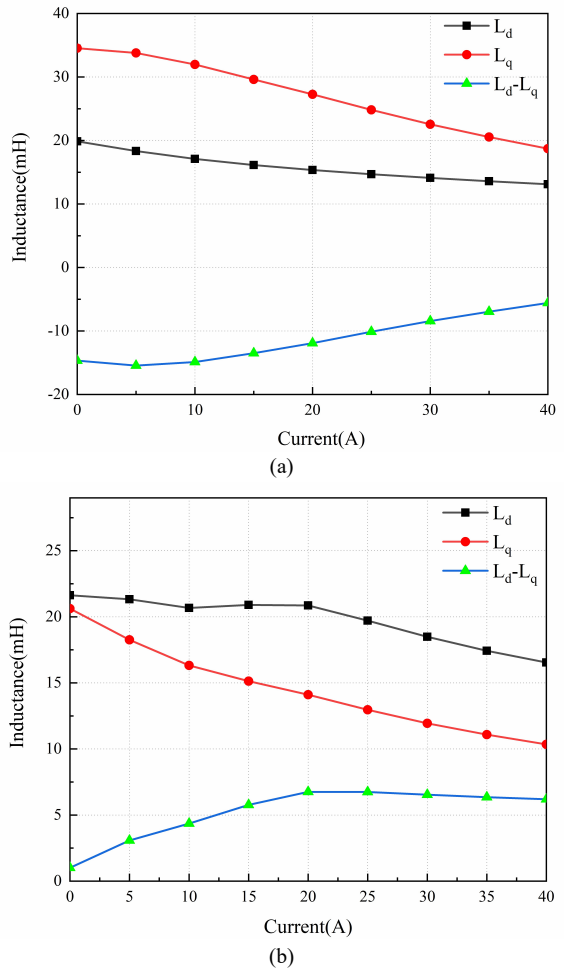

Fig. 10. Inductance characteristics. (a) CVTSM. (b) VLF-RSPM.

D. Torque Production

The inductance characteristics of the VLF-RSPM and the CVTSM have been analyzed above, and now the torque characteristics are analyzed. In addition to the given current, the torque is also related to the *d-q* axis inductance, which can be expressed as follows

$$\begin{aligned} T_e &= \frac{3P}{2}\left[\psi_m i_q + (L_d - L_q) i_d i_q\right] \\ &= \frac{3P}{2}\left[\psi_m I_s \cos(\beta) + (L_d - L_q) I_s^2 \cos(\beta)\sin(-\beta)\right] \end{aligned} \tag{6}$$

Where Ψ_m is the EMF of PM, I_s is the magnitude of the given current, and β is the angle of the given current. According to Equ. 6 and the inductance of the above two motors, the current angle should be positive when CVTSM torque is at its maximum, and the current angle should be negative when the VLF-RSPM torque is the largest, which can be verified in Fig. 11. When the current Angle is -3°, the torque of the VLF-RSPM reaches the maximum value of 88Nm, and when the current Angle is 40° , the torque of the CVTSM reaches the maximum value of 102Nm. Therefore, the output torque capacity of VLF-RSPM is significantly lower than that of CVTSM, which is also a defect caused by the addition of magnetic barriers. In addition, torque fluctuation is also a very important performance of the motor [19]. Fig. 12 shows the torque fluctuation of the two motors. It is observed that the torque fluctuation of VLF-RSPM is less than that of CVTSM, which is 17% for CVTSM and 8% for VLF-RSPM, mainly due to the addition of three magnetic barriers in VLF-RSPM.

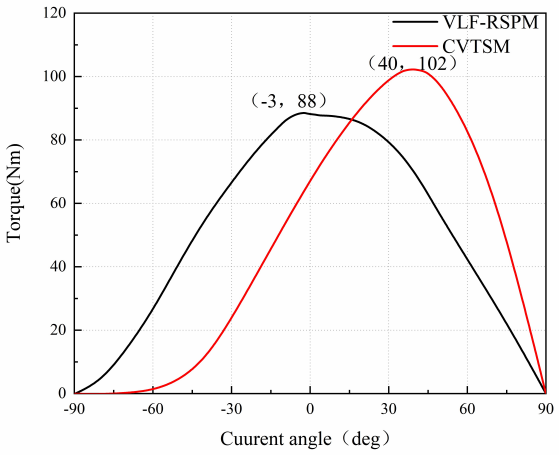

Fig. 11. Output torque versus current angle.

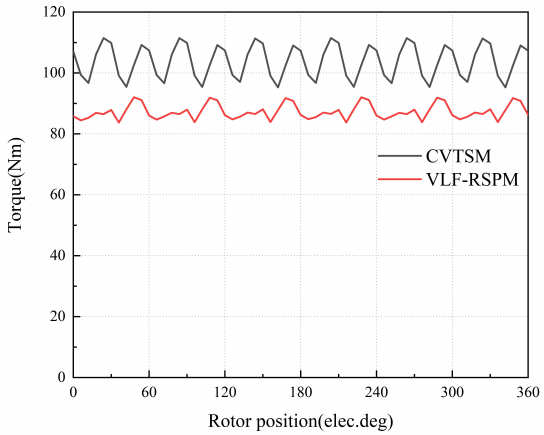

Fig. 12. Torque ripple.

E. Evaluating the Irreversible Demagnetization Risk

At present, many scholars use simulation methods to evaluate the DIR of PMs [20]. In this paper, the magnetization state of PM's working point is calculated. Fig. 13 shows the magnetization state of the working points selected by each motor under no-load conditions. The CVTSM selects three observation points, and the VLF-RSPM selects four observation points. Fig. 14 is the magnetic flux density of the VLF-RSPM and the CVTSM at the observation points under no-load conditions. Fig. 15 is the flux density of each observation point when the VLF-RSPM and the CVTSM are running at low speed; Fig. 13 is the flux density of each observation point when the two motors rotate at 6000 rpm.

Fig. 14 (a) shows that the flux density of the three observation points of CVTSM have a very small difference, which can be regarded as the same, which is about 1.098 T; the magnetic flux density of VLF-RSPM has no difference. The flux density at observation point B reaches a maximum of about 1.06 T, and the flux density at observation point A reaches a maximum of about 0.97 T, as shown in Fig. 14(b). It shows that the magnetization states of the PMs of the two motors are almost the same.

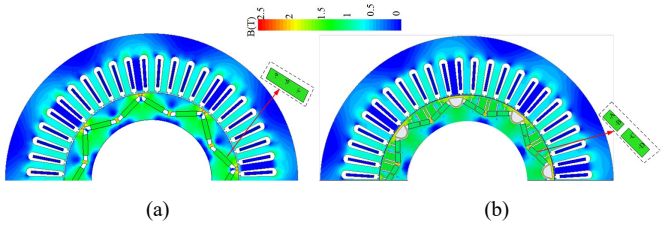

(a) (b)

Fig. 13. Flux density distributions under no-load conditions. (a) CVTSM. (b) VLF-RSPM.

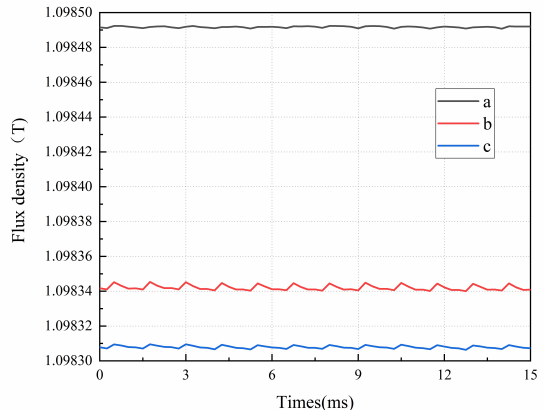

(a)

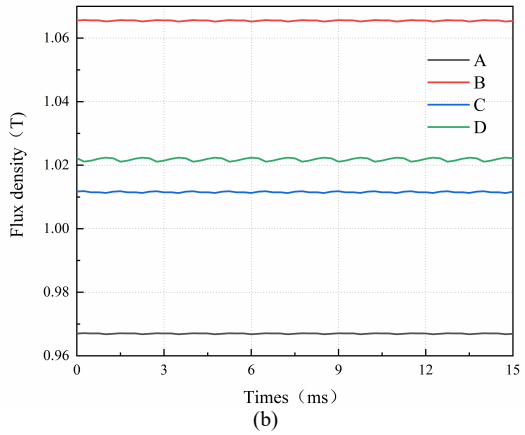

(b)

Fig. 14. Flux density variation curves under no-load conditions. (a) CVTSM. (b) VLF-RSPM.

The motors are in a state of enhanced magnetic field when it runs at low speed. Since the VLF-RSPM has the characteristics of $L_d > L_q$, in Fig. 15, the VLF-RSPM applies a positive i_d of 30 A, and CVTSM applies a negative i_d of 30 A. Comparing the flux density of each observation point in Fig. 15 (a) and Fig. 15(b), it is obvious that the PM Flux density of VLF-RSPM is higher than that of CVTSM, which indicates that VLF-RSPM has a lower IDR in the enhanced magnetic field state. Fig. 16 shows the flux density of the VLF-RSPM and the CVTSM under the condition that the rotation speed is 6000 rpm turntable, that is, the motor is in a weak magnetic state. It can be seen from the figure that the PM density of VLF-RSPM is

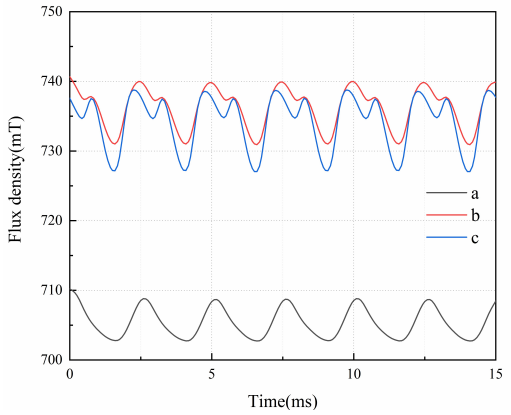

(a)

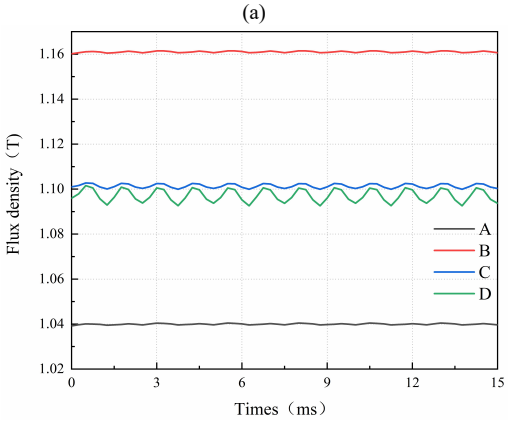

(b)

Fig. 15. Flux density variation curves under heavy load conditions. (a) CVTSM.(b) VLF-RSPM.

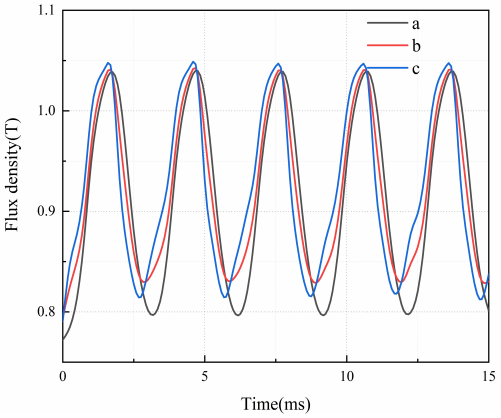

(a)

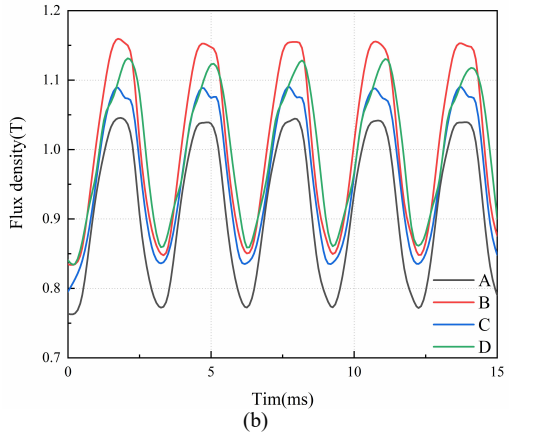

Fig. 16. Flux density at the same speed of 6000 rpm. (a) CVTSM. (b) VLF-RSPM.

higher than CVTSM, which indicates that the VLF-RSPM also has a lower IDR in the weak magnetic state.

In summary, the VLF-RSPM has a low IDR whether in the magnetic field enhancement state or the weak magnetic state.

F. Output Power and Torque Versus Speed Characteristics

The flux-weakening ability of the motor determines the speed control ability, to broaden the speed control range of the motor, it needs a good weak magnetic ability. To verify the positive VLF-RSPM has a better speed expansion ability, the flux-weakening capacity of the two motors is analyzed and compared. The flux-weakening coefficient is defined as

$$k_{wm} = \frac{L_d \cdot I_{\lim}}{\psi_{pm}} \tag{7}$$

Ψ_{pm} is the PM flux, and I_{lim} is the limit current at the maximum magnetic flux leakage. Table III shows L_d and Ψ_{pm} of the two motors. According to the formula (7), the k_{wm} of VLF-RSPM is obviously greater than CVTSM, and it can also be verified from Fig. 17 that VLF-RSPM has stronger speed expansion ability.

In this paper, by comparing the performance of the wide speed regulation performance of the VLF-RSPM and the CVTSM, it is verified that the designed motor has a strong flux-weakening ability and a wide speed regulation range. From the torque-speed diagram shown in Fig. 17 (a), the output torque of CVTSM is 102 T larger than that of the VLF-RSPM in the low-speed operating region by 14T, and in the high-speed operating region, the maximum speed of CVTSM only reaches only 6250 rpm, while the maximum speed of VLF-RSPM reaches 10000rpm, mainly because VLF-RSPM has 24% controllable magnetic flux leakage. In addition, Fig. 17(b) shows the output power-rotation speed diagram. In the low-speed operation area, although the output power of CVTSM is slightly higher than that of the VLF-RSPM, the constant power speed regulation range of VLF-RSPM is significantly larger than that of the CVTSM. The main reason for this is the L_d>L_q characteristic of VLF-RSPM.

G. Iron Loss and Efficiency Analysis

High efficiency is a very important motor performance index of the motor, and loss is the main factor affecting the efficiency of the motor. However, from Table I, it can be found that the

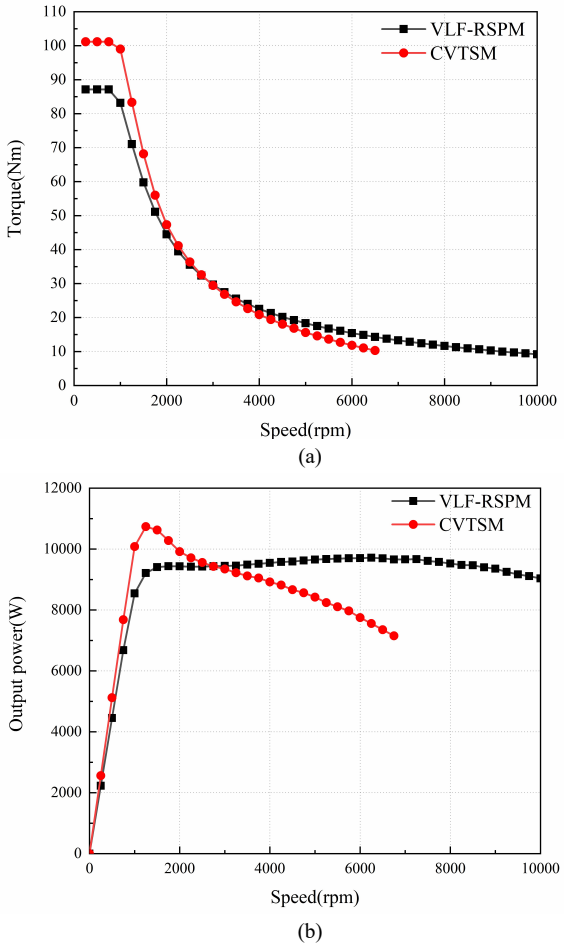

Fig. 17. (a) Torque-speed. (b) Output power-speed.

TABLE III
THE PERFORMANCE COMPARISON

Items	VLF-RSPM	CVTSM
Maximum torque (Nm)	88	102
Torque ripple (%)	8	17
Maximum speed (rpm)	10000	6750
Maximum iron Loss (kW)	0.192	0.54
Constant power region (rpm)	2000-8000	/
High-speed time noise (dm)	35.32	41.08
L_d (mH)	16.2	14.8
Ψ_{pm} (Wb)	0.51	0.59
k_{wm}	0.95	0.75

parameters of the VLF-RSPM and the CVTSM are the same, so the copper loss, mechanical loss, and impurity loss of the VLF-RSPM and the CVTSM are not much different. Therefore, this section mainly analyzes the iron loss and efficiency of the VLF-RSPM and the CVTSM by adopting the FEA.

Fig. 18 is the Map of iron loss of the VLF-RSPM and the CVTSM. In the low-speed region, the iron loss of the VLF-RSPM and the CVTSM is not much different. In the high-speed region, the maximum iron loss of VLF-RSPM is 0.192kW at the speed of 10,000 rpm while the iron loss of CVTSM is 0.54kW at the speed of 6,000 rpm much higher than that of the VLF-RSPM. This is because the VLF-RSPM has a large amount of leakage flux in the high-speed weak magnetic field, thereby reducing the loss.

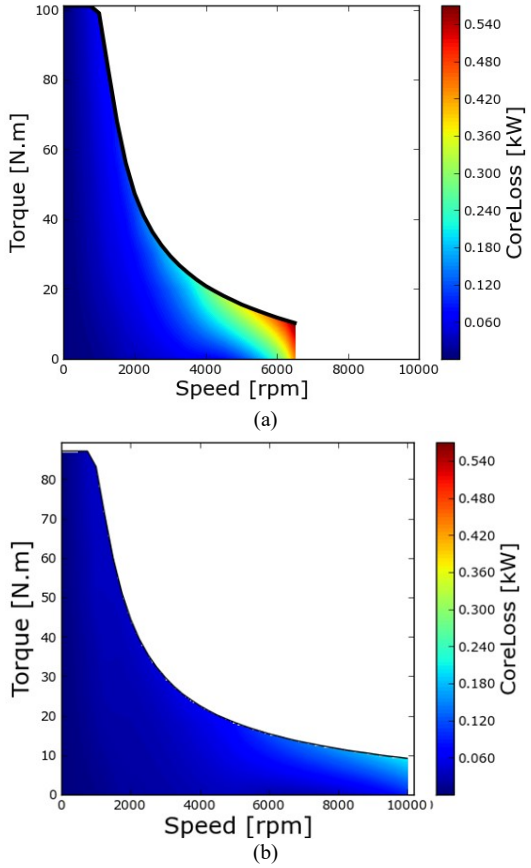

Fig. 18. Iron loss. (a) CVTSM. (b) VLF-RSPM.

Fig. 19 is the efficiency Map of the VLF-RSPM and the CVTSM. By comparing Fig. 16 (a) and (b) can be found that the maximum efficiency of VLF-RSPM is 97% distributed at 0~2500 rpm, which is higher than that of CVTSM, and the CVTSM has a maximum efficiency of 96% distributed from 0 than that of CVTSM, and the efficiency of VLF-RSPM is higher in the overall range. Due to the magnetic flux leakage characteristics of VLF-RSPM, the loss is reduced and the efficiency is increased.

H. Stress Analysis

When the motor runs at high speed, a huge centrifugal force will be generated, which will deform or even break the relatively fragile parts of the rotor structure of the motor. Therefore, analyzing the stress of the VLF-RSPM and the

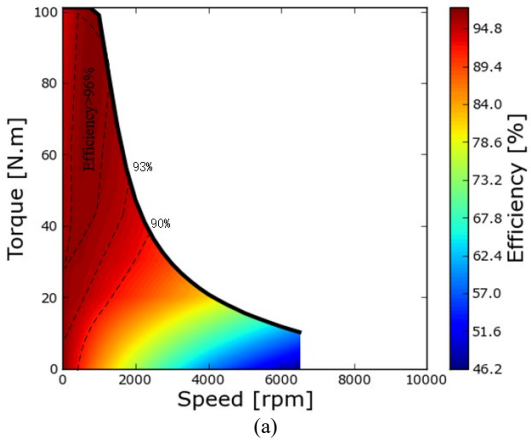

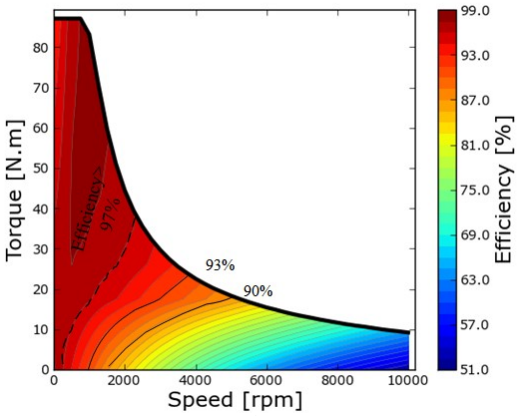

Fig. 19. The efficiency. (a) CVTSM. (b) VLF-RSPM.

CVTSM is very necessary. Fig. 20 is a diagram of the mechanical stress of the rotors of the VLF-RSPM and the CVTSM at a temperature of 25° and a rotational speed of 10,000 rpm. The fracture strength of silicon steel is 450 Mpa, which is far greater than the maximum stress of the VLF-RSPM and the CVTSM, and the maximum stress of the VLF-RSPM and the CVTSM are located in the magnetic bridge part. Fig. 20 (c) shows that although the stress of VLF-RSPM is larger than that of CVTSM at all speeds, it is far less than the maximum stress of magnetic steel, and it also shows that both motors can operate safely within the full speed range.

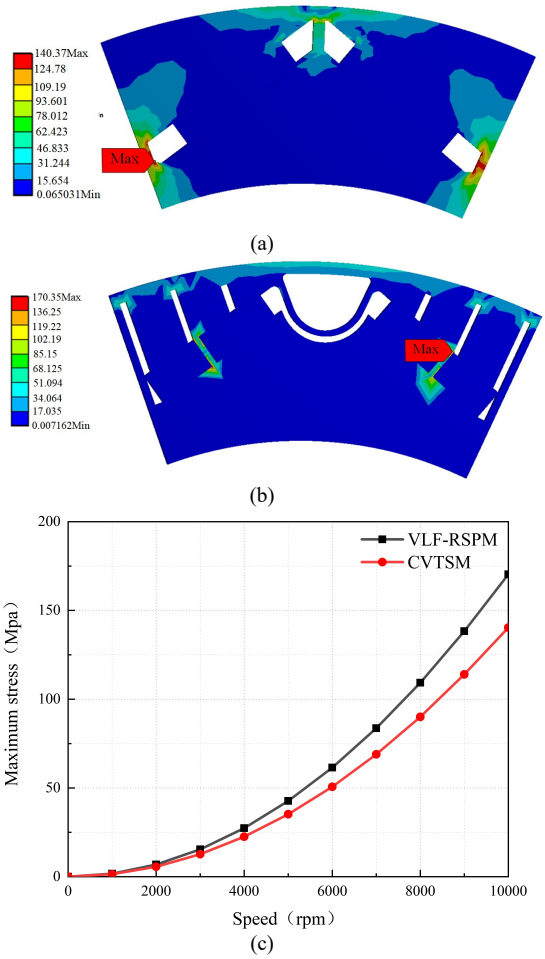

Fig 20. Stress analysis at a temperature of 25° and a speed of 10000rpm. (a) CVTSM. (b) VLF-RSPM.(c) Stresses at different speeds.

I. Noise Analysis

Weight sound pressure level is used as the evaluation standard of electromagnetic noise during motor operation. Fig. 21 shows the distribution of sound pressure weight levels of two motors at 1000Hz. Comparing Fig. 21(a) and (b), the sound pressure level of VLF-RSPM at high speed is significantly lower than that of CVTSM. Fig. 22 shows the variation of noise and sound pressure of the two motors with frequency. It can be seen from Fig. 22 (a) that noise intensity increases with the increase of frequency, but the change in noise intensity is small when the frequency is greater than 700Hz. Fig. 22(b) shows that the variation trend of sound pressure is consistent with that of noise intensity. In addition, the overall noise intensity and sound pressure of VLF-RSPM are lower than those of CVTSM, mainly because the magnetic barrier set by the VLF-RSPM can effectively reduce the noise of the motor during operation. The noise simulation of the two motors adopts the shell and stator model as shown in Fig. 23, and the materials are structural steel.

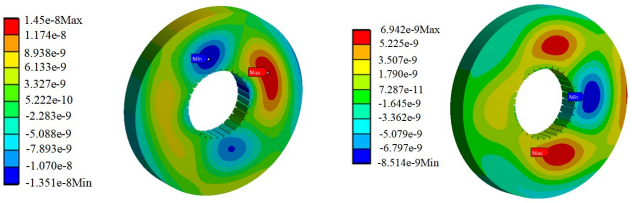

(a) (b)

Fig. 21. Weight sound pressure level. (a) CVTSM. (b) VLF-RSPM.

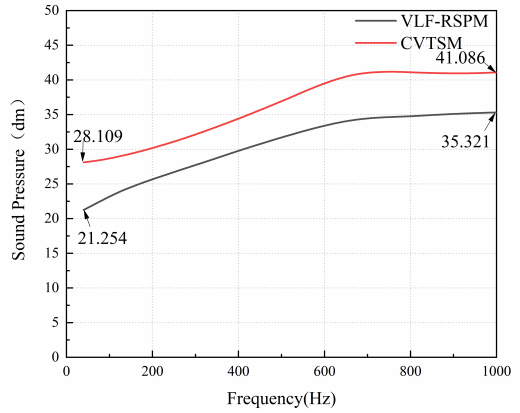

(a)

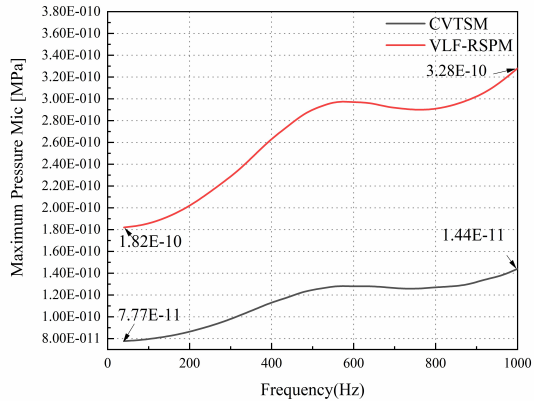

(b)

Fig. 22. The noise varies with frequency. (a) Sound Pressure-Frequency. (b) Maximum Pressure Mic-Frequency.

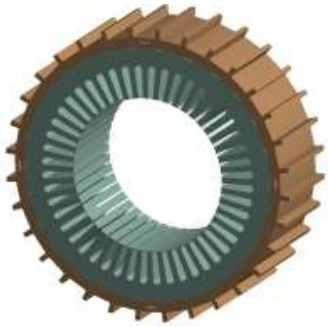

Fig. 23. The employed model of two motors.

IV. Conclusion

In this paper, a new VLF-RSPM motor is presented. The innovation is to realize both reverse salient-pole characteristics and variable leakage flux characteristics by using a method of adding magnetic bridges and magnetic barriers. The electromagnetic performance and noise of VLF-RSPM and CVTSM are analyzed and compared by the FES. The results show the VLF-RSPM has the advantages of small torque ripple, high efficiency, low noise, strong flux-weakening ability, wide speed range, and low IDR of PM. Meanwhile, it meets the requirements of mechanical strength. Therefore, the proposed VLF-RSPM verifies the rationality and effectiveness of the design idea and solves problems such as the difficulty of expanding the speed of traditional motors.

References

[1] J. Mielczarek, “Mobility Turnaround, Air Pollution Control and Secure the Budget-Electric Mobility in the Urban Area of Tension,” in *Proc. of 2019 Electric Vehicles International Conference (EV)*, Bucharest, Romania, 2019, pp. 1-5.

[2] S. S. Reddy Bonthu, M. Z. Islam, and S. Choi, “Performance Review of Permanent Magnet assisted Synchronous Reluctance Traction Motor Designs,” in *Proc. of 2018 IEEE Energy Conversion Congress and Exposition (ECCE),* Portland, USA, 2018, pp. 1682-1687.

[3] A. Campeanu, M. A. Enache, and I. Vlad *et al*, “Comparative Dynamic Performance Analysis of Line-start Synchronous Motors with Electromagnetic and Permanent-Magnet Excitation. A Review,” in *Proc. of 2019 11th International Symposium on Advanced Topics in Electrical Engineering (ATEE)*, Bucharest, Romania, 2019, pp. 1-8.

[4] M. A. Darmani, E. Pošković, and F. Franchini *et al*, “Multiple Layer Magnetic Materials for Variable Flux Permanent Magnet Machines,” in *Proc. of 2020 International Conference on Electrical Machines (ICEM)*, Gothenburg, Sweden, 2020, pp. 1662-1668.

[5] X. Zhu, W. Wu, and S. Yang *et al*, “Comparative Design and Analysis of New Type of Flux-Intensifying Interior Permanent Magnet Motors With Different Q-Axis Rotor Flux Barriers,” *IEEE Transactions on Energy Conversion*, vol. 33, no. 4, pp. 2260-2269, Dec. 2018.

[6] X. Zhu, S. Yang, and Y. Du *et al*, “Electromagnetic Performance Analysis and Verification of a New Flux-Intensifying Permanent Magnet Brushless Motor With Two-Layer Segmented Permanent Magnets,” *IEEE Transactions on Magnetics*, vol. 52, no. 7, pp. 1-4, July 2016, Art no. 8204004.

[7] M. Kashif and B. Singh, “Design of a New Spoke-PMSM with Multiple Flux Barriers Considering Flux-Intensifying Effect for SWPS,” in *Proc. of 2021 IEEE 12th Energy Conversion Congress & Exposition-Asia (ECCE-Asia)*, Singapore, 2021, pp. 521-525.

[8] X. Wang, Z. Wan, and M. Zhao *et al*, “Performance of an Axial Flux Hybrid Excitation Motor with SMC for HEVs,” in *Proc. of 2020 IEEE International Conference on Applied Superconductivity and Electromagnetic Devices (ASEMD)*, Tianjin, China, 2020, pp. 1-2.

[9] L. Zhang, Y. Fan, and C. Li *et al*, “Design and Analysis of a New

Six-Phase Fault-Tolerant Hybrid-Excitation Motor for Electric Vehicles," *IEEE Transactions on Magnetics*, vol. 51, no. 11, pp. 1-4, Nov. 2015.

[10] X. Yang, Y. Liu, and W. Chen *et al*, "Sandwich-Type Multi-Degree-of-Freedom Ultrasonic Motor with Hybrid Excitation," *IEEE Access*, vol. 4, pp. 905-913, 2016.

[11] X. Zhu, Z. Xiang, and L. Quan *et al*, "Multimode Optimization Design Methodology for a Flux-Controllable Stator Permanent Magnet Memory Motor Considering Driving Cycles," *IEEE Transactions on Industrial Electronics*, vol. 65, no. 7, pp. 5353-5366, July 2018.

[12] Y. Xie, Z. Ning, and Z. Ma *et al*, "Design and Research of Novel Variable Flux Memory Motor with Series Hybrid Magnets," in *Proc. of 2020 23rd International Conference on Electrical Machines and Systems (ICEMS)*, China, 2020, pp. 2142-2147.

[13] H. Yang, H. Lin, and J. Dong *et al*, "Analysis of a Novel Switched-Flux Memory Motor Employing a Time-Divisional Magnetization Strategy," *IEEE Transactions on Magnetics*, vol. 50, no. 2, pp. 849-852, Feb. 2014.

[14] Y. An, H. Wen, and Z. Meng *et al*, "Performance analysis of novel magnet arrayed permanent magnet synchronous motor based on ANSOFT," in *Proc. of 2010 International Conference on Intelligent Control and Information Processing*, Dalian, China, 2010, pp. 715-718.

[15] O. Payza, Y. Demir and M. Aydin, "Investigation of Losses for a Concentrated Winding High-Speed Permanent Magnet-Assisted Synchronous Reluctance Motor for Washing Machine Application," *IEEE Transactions on Magnetics*, vol. 54, no. 11, pp. 1-5, Nov. 2018.

[16] F. Liu, L. Quan, and X. Zhu *et al*, "Investigation of Reverse Saliency Characteristic in Flux-Intensifying Hybrid Permanent Magnet Motor Considering Various Operation Conditions," in Proc. *of 2018 IEEE International Conference on Applied Superconductivity and Electromagnetic Devices (ASEMD)*, Chengdu, China, 2018, pp. 1-2.

[17] X. Qian, G. Xiaorui, and Q. Haihong *et al*, "Research on the Application of Flux-Weakening Control in PMSM with Wide Range Speed Variation," in *Proc. of 2017 International Conference on Smart Grid and Electrical Automation (ICSGEA)*, Changsha, China, 2017, pp. 371-374.

[18] W. Zhu, X. Liu, and G. Guo *et al*, "Design and evaluation of a novel controllable leakage flux permanent magnet motor with wide speed ranges," in *Proc. of 2021 IEEE 4th* International *Electrical and Energy Conference (CIEEC)*, Wuhan, China, 2021, pp. 1-4.

[19] X. Deng, B. Mecrow, and H. Wu *et al*, "Design and Development of Low Torque Ripple Variable-Speed Drive System With Six-Phase Switched Reluctance Motors," *IEEE Transactions on Energy Conversion*, vol. 33, no. 1, pp. 420-429, March 2018.

[20] B. Ma, G. Lei, and J. Zhu *et al*, "Application-Oriented Robust Design Optimization Method for Batch Production of Permanent-Magnet Motors," *IEEE Transactions on Industrial Electronics*, vol. 65, no. 2, pp. 1728-1739, Feb. 2018.

Xiping Liu received his B.S. degree from Hohai University, Nanjing, China, in 1999; his M.S. degree from the Jiangxi University of Science and Technology, Ganzhou, China, in 2004; and his Ph.D. degree in Electrical Engineering from Southeast University, Nanjing, China, in 2009. He is presently working as a Professor in the Department of Electrical Engineering and Automation, Jiangxi University of Science and Technology. His current research interests include the analysis and design of permanent magnet synchronous machine, and wind power technology.

Siting Zhu was born in China, in 1996, she received her B.S. degree from Jiangxi University of Science and Technology, Ganzhou, China, in 2016. She is presently working towards her M.S. degree in Electrical Engineering at Jiangxi University of Science and Technology. Her current research includes design and analysis of PMSMs, and the intensifying-flux of variable leakage flux PMSMs.

Dabin Liu was born in China in 1994, he received his B.S. degree from Nanchang University, Nanchang, China, in 2015; He is presently working toward his M.S. degree in Electrical Engineering at the Jiangxi University of Science and Technology, Ganzhou, China. His current research interests include the design of permanent magnet motors, the interior PMSMs and their control method.

Jianwei Liang was born in China. He received his B.S. degree from Jiangxi University of Science and Technology, Ganzhou, China; his M.S. degree from the Nanchang University, Nanchang, China. He is presently working as an Associate Professor at the Jiangxi University of Science and Technology. His current research interests include PMSMs, and their drive and control.